metals

MDPI

Article

Induction Weld Seam Characterization of Continuously Roll Formed TRIP690 Tubes

Alexander Bardelcik * and Bharathwaj Thirumalai Ananthapillai

School of Engineering, College of Engineering and Physical Sciences, University of Guelph, Guelph, ON N1G 2W1, Canada; banantha@uoguelph.ca

* Correspondence: abardelc@uoguelph.ca; Tel.: +1-519-824-4120

Received: 5 March 2020; Accepted: 20 March 2020; Published: 25 March 2020

Abstract: The weld seam characteristics of continuously roll formed and induction seam welded TRIP690 tubes were examined in this work. These tube are subsequently used in automotive hydroforming applications, where the weld seam characteristics are critical. The induction seam welds are created through a solid-state welding process and it was shown that by increasing the induction frequency by 26%, the weld seam width within the heat affected zone (HAZ) reduced due to a plateau in the hardness distribution which was a result of a delay in the transformation of martensite. 2D hardness distribution contours were also created to show that some of the weld conditions examined in this work resulted in a strong asymmetric hardness distribution throughout the weld, which may be undesirable from a performance perspective. An increase in the pressure roll force was also examined and revealed that a wider total weld seam width was produced likely due to an increase in temperature which resulted in more austenitization of the sheet edge prior to welding. The ring hoop tension test (RHTT) was applied to the tube sections created in this work. A Tensile and Notch style ring specimen were tested and revealed excellent performance for these welds due to high peak loads (~17.2 kN) for the Notch specimens (force deformation within weld) and lower peak loads (~15.2 kN) for the Tensile specimens for which fracture occurred in the base metal.

Keywords: induction welding; roll forming; TRIP690; metallography; microhardness testing; ring hoop tension test

1. Introduction

In order to combat the effects of vehicle greenhouse gas emissions on global warming, the Corporate Average Fuel Economy (CAFÉ) standards [1] were enacted by the United States administration and research activity into vehicle lightweighting of body-in-weight (BIW) structures has been targeted by automakers. One of the methods used to reduce BIW weight has been the development and implementation of Advanced High Strength Steel (AHSS), which allows for down gauging of sheet metal thickness while maintaining high crash performance standards [2]. Some of the candidate AHSS steels include Dual-Phase (DP), Complex Phase (CP), Transformation Induced Plasticity (TRIP) and Quench and Partitioned (Q&P) steels. Another approach to BIW lightweighting is through the implementation of innovative metal forming manufacturing processes such as: (1) press hardening of steel [3] and high strength aluminum alloys [4]; (2) warm forming of aluminum [5] and magnesium [6]; and (3) hydroforming of tubular steel [7]. Hydroforming of AHSS takes advantage of both lightweighting methods, making it an attractive process for OEMs. Therefore, the focus of this work will be on the seam weld characterization of TRIP690 straight tubular stock that has been manufactured for hydroforming applications. The proceeding sections will highlight the significant deficit within the literature on the topic of thin gauge roll formed tubes that have been induction seam welded. In particular, the effect of the induction weld frequency on the resultant weld microstructure

will be explored, along with the development of a mechanical test to evaluate the fracture performance of these complex TRIP690 weld seams.

1.1. Hydroforming

Tubular hydroforming is now a mature metal forming technology in which a continuous tubular section is pressurized with a liquid media and formed to the cross-section of a die as shown in Figure 1 for the high-pressure [8] and low-pressure [9] hydroforming processes. Continuously roll formed and seam welded tube stock is the most commonly used in automotive hydroforming applications. Tube pre-bending operations, such as precision mandrel rotary-draw, are used to first pre-bend the straight tubes prior to the hydroforming process as shown in Figure 1a. Significant amounts of strain hardening that are imposed on the tube during pre-bending must be considered when designing the subsequent hydroforming process [10], as the non-linear strain path of the deformation may lead to premature fracture [11]. This is especially true for the weld seam, which in some situations is located along the tubular cross-section where pre-bending and hydroforming may impose significant strains that can lead to premature failure (or burst) due to the strength and ductility differential between the weld and base metal.

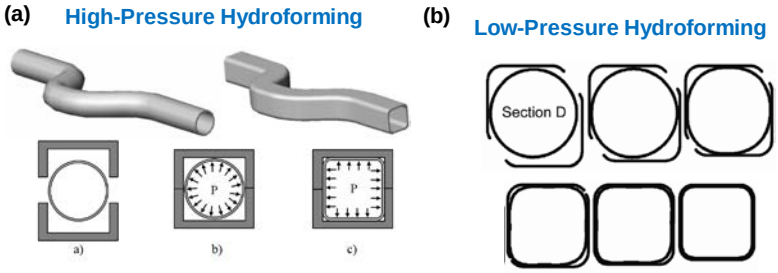

Figure 1. (**a**) High [8] and (**b**) low pressure hydroforming [9].

1.2. Tubular Roll Forming

The tube stock commonly used in hydroforming is manufactured using the continuous tubular roll forming process. This is a continuous process in which a sheet metal strip is deformed into a circular profile by passing it through a series of roll forming stages in succession as shown in the Figure 2 schematic. The roll forming process is followed by a seam welding station, in which the tubular section is closed using high-frequency induction, laser or tungsten inert gas (TIG) welding processed. A final calibration of the cross-sectional geometry is then conducted, followed by cutting of the tube [12,13]. In addition to the consistency of the wall thickness in the finished tube product, the quality of the weld seam is of critical importance for the subsequent pre-bending and hydroforming process which these tubes will undergo. Although they do not specify the welding process used, Groche et al. [12] showed that continuous roll forming resulted in a weld seam thickness that is greater than the average cross-sectional thickness of the tube due to the force applied to the edges of the sheet during welding. This results in base metal failure when the tubes were subject to free-expansion bulge tests. Through finite element simulation, Groche and Breitenbach P [13] showed that the vertical leveling strategy (W) roll forming process could be used to enhance the thickness of the tube near the seam weld for enhanced performance during hydroforming.

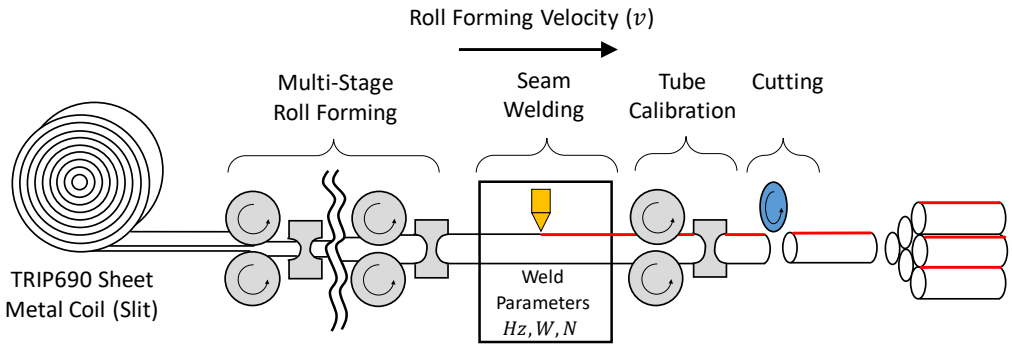

Figure 2. A schematic of the tubular roll forming process.

1.3. Induction Seam Welding in Roll Forming

Induction welding (or high frequency induction, HFI) is the most common seam welding process used in the roll forming process due to the high production rates and robust production characteristic of this process [14,15]. During the induction welding process, a tube passes through an induction coil with a gap between the sheet edges that is then closed at the weld rolls (or pressure rolls), which apply a squeeze pressure to the tube edge as shown in Figure 3. This welding process is a form of resistance welding due to the sheet edges heating (due to skin effect and proximity effect) as a result of a high frequency current induced on the work piece. The skin effect is a phenomenon that causes the high frequency current to stay close to the surface of the tube prior to closing the gap, while the proximity effect causes the current to intensify as the gap between the tube edges decreases, thus resulting in the highest temperature as the tube edge is forced together at the pressure rolls [14–18]. The temperature of the tube edge does not exceed the liquidus temperature of the metal, therefore induction welding is also referred to as a forge welding process, which can be classified as a solid-state welding process. In order to complete this type of a solid-state weld, a squeeze force must be applied to the two edges of the tube to form a joint [14].

Considering these aspects of the induction seam welding process, the induction coil power (kW) frequency (kHz) and other parameters as shown in Figure 3, must also be carefully set in order to achieve a sound weld. In terms of thin gauge automotive tube, there is little to no published literature on the topic, but there has been some activity in roll forming of heavy gauge pipes. In roll formed pipeline steel Kim and Kim [19] showed that increased weld power resulted in higher temperatures at the weld seam. This had the effect of changing the gap at the point of contact. Ghaffarpour et al. [15] modified the edge condition of a 5 mm thick sheet metal in order to reduce the temperature gradient at the seam weld and improve the final weld microstructure. Numerical work to simulate the induction welding process has led to the development of complex finite element (FE) models of the roll forming induction welding process in which the coupled thermal and electromagnetic processes are modeled to predict the thermal condition at the tube edge [15,18]. Okabe et al. [20] enhanced these models by also coupling the elastic-plastic behavior of the metal within the FE models to predict wall thickening for a continuously roll formed pipeline steel. Paul [16] simulated the roll forming and induction welding of a thin-walled 1.27 mm thick low carbon steel tube and predicted that a 400 kHz induction welding frequency resulted in a superior weld when compared to a tube welded at 200 kHz, which resulted in a wider and less desirable HAZ. Although not directly related to induction welding of roll formed tubes, recently developed analytical models used to predict the temperature distribution generated due to planar induction heating can be a very useful and efficient tool in understanding the effect that induction heating parameters have on thin sheet metal [21,22].

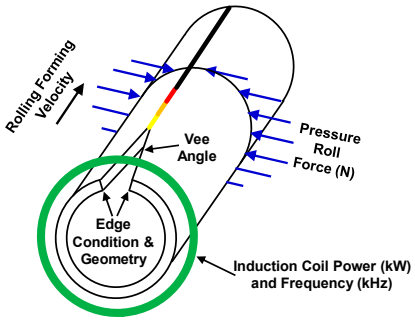

Figure 3. A schematic of the process parameters involved in induction seam welding.

1.4. Welding of TRIP Steels

The Transformation Induced Plasticity (TRIP) effect in steels was first observed in the work of Zakay et al. [23] and the commercialized by Nippon Steel [24] as a class of steels which contained some volume fraction of retained austenite (γ) within a multi-phase microstructure that includes ferrite (α) and may include martensite (α') and bainite (α_B). The excellent strength and ductility properties of these AHSS steels are a result of the TRIP effect during plastic deformation (or loading), which results in the transformation of the γ into α', thus delaying the onset of necking due to enhanced strain hardening. These properties make TRIP steels very desirable for vehicle BIW energy absorbing applications and when coupled with the hydroforming process, an excellent opportunity for lightweighting can be realized. This is in fact the motivation for the current research, where the development of continuously roll formed and induction seam welded TRIP690 tube stock was investigated. The main focus of this work will be the effect of induction welding frequency and pressure roll force on the seam weld characteristics of roll formed tubes, which to the authors' knowledge has not been explored academically in the literature. In addition, a mechanical test to assess the performance of the seam welds of the roll formed tube stock was developed to test the welds created for this work.

Although there is no literature available on the topic of induction seam welded TRIP steel, there has been considerable research conducted on the fusion (Resistance Spot Welding-RSW, Gas Metal Arc Welding-GMAW and laser welding) and solid-state (friction stir welding FSW and ultrasonic) welding of TRIP alloys. RSW of a high strength TRIP steel was shown to be susceptible to weld defects due to the rich chemistry and thermophysical properties of the material [25]. Sajjadi-Nikoo et al. [26] showed that a fully martensitic RSW nugget for a TRIP alloy resulted in poor cross-tension test performance due to interfacial failure, which was remedied through post weld heat treatments that tempered the fusion zone nugget. Spena et al. [27] spot welded (using optimal parameters) TRIP and Q&P AHSS alloys and showed that the HAZ for these alloys were void of the initial retained austenite of the base metal. Zhang et al. [28] used GMAW to weld a TRIP600 (ferrite, retained austenite and bainite BM) and showed that the weld exhibited excellent mechanical and impact properties due to the microstructural make-up of the fine grained HAZ, which consisted of ferrite and granular bainite. Lopez Cortez et al. [29] also found that the HAZ of a GMAW welded TRIP800 automotive steel consisted of a mixed ferrite (polygonal) and bainite (lower), while the fusion zone consisted of martensite and some ferrite (Widmanstatten and allotriophic) and bainite (upper). Grachar et al. [30] laser welded an automotive TRIP (ferrite with bainite-austenite BM) and revealed that the microstructure within the inter-critical HAZ (ICHAZ) consisted of ferrite and areas consisting of lath bainite-martensite-austenite. The austenite was also shown to have transformed into martensite-austenite (M-A) islands due to the inter-critical heating within this ICHAZ. The microstructure within the fine-grained (FGHAZ) and coarse-grained (CGHAZ) predominantly consisted of a martensitic-bainitic microstructure.

Like induction seam welding, friction stir welding (FSW) is a solid-state welding process as well. Medina et al. [31] conducted FSW trials on a TRIP780 (ferrite-bainite-retained austenite BM) alloy and characterized the weld microstructure to show a predominantly martensitic stir zone (SZ) and a HAZ which nearly matched the BM microstructure. They also found an increase in retained

austenite content within the SZ and HAZ when compared to the BM. Mironov et al. [32] joined a high strength 1.2 GPa automotive TRIP alloy using FSW. The microstructure within the HAZ of this material revealed a reduction in retained austenite content, which was suspected to have transformed into bainite (resulting in softening), while the SZ was predominantly martensitic. Mazzaferro et al. [33] applied friction stir spot welding (FSSW) to TRIP800 sheets and observed the transformation of the retained austenite into coalesced bainite within the thermo-mechanically affected zone, which is within the intercritical temperature range.

2. Materials and Methods

2.1. TRIP690 Material Properties

In this work, a grade of TRIP690 sheet metal with a nominal thickness of 1.6 mm was roll formed into 2" (~50.8 mm) OD tubes. The base metal (BM) microstructure for this material is shown in Figure 4a and consists of a ferritic matrix with retained austenite as shown by the elevated and featureless hard phase in the SEM micrograph. The nominal hardness of the BM is 250 HV_{300}. There also exists a small volume fraction of martensite and bainite, but these are nearly negligible. Uniaxial tensile specimens (2" gauge length, ASTM E8 type) were extracted from the roll formed tubes along the longitudinal tube direction (see Figure 4 inset) and the nominal engineering stress vs. strain curve for this material is shown in Figure 4b. The nominal yield strength, tensile strength and total elongation from repeat tensile tests is 570 MPa, 758 MPa and 0.24, respectively.

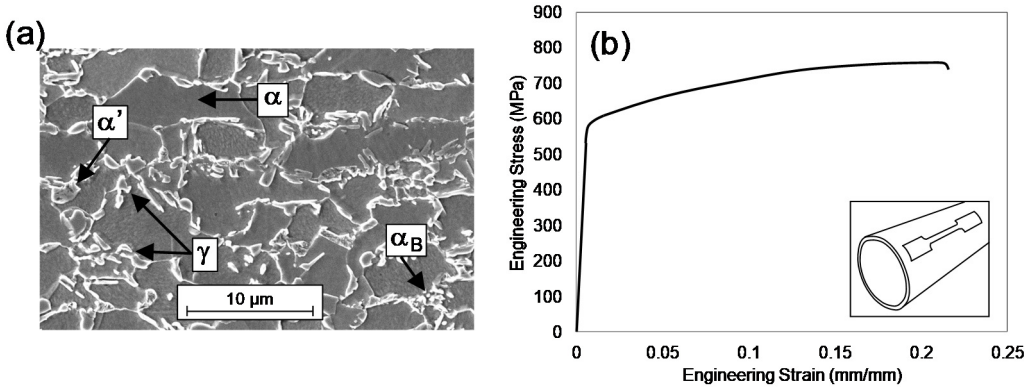

Figure 4. (**a**) TRIP690 base metal microstructure (α-Ferrite, γ- Retained Austenite, α'-Martensite, α_B-Bainite); (**b**) A representative engineering stress versus strain curve from a single uniaxial tensile test on a TRIP690 tubular specimen.

2.2. Tubular Roll Forming Parameters

An industrial tubular roll forming apparatus was used to produce the tubular specimens that are examined in this work. During a single continuous run of the TRIP690 material the tube was roll formed using a constant roll forming velocity. The vee angle, edge condition, weld power (±1% variation) and pressure roll force (±2% variation) was held constant as well (see Figure 3). Based on all of the induction welding parameters used, the industrial roll forming welding controller computed the weld power for this experimental setup. The effect of induction weld frequency was examined in this work and three separate specimens were manufactured and labeled LOW, MED and HIGH, which represented a relative weld frequency of 1.0, 1.17 and 1.26, respectively as shown in Table 1. The LOW weld frequency was less than 300 kHz, as reported by the tube manufacturer. In addition to these three specimens, a HIGH_PRF specimen was also produced and represents a condition where the pressure roll force (PRF) was increased by 14%, while the weld power was decreased by ~7% and weld frequency was increased by 9% in order to observe the effect that pressure roll force (plus lesser contributions from power and frequency) has on the weld seam characteristics. A non-contact temperature probe is used to monitor the weld seam temperature during the roll forming process. The relatively crude

measurement was used to confirm that the weld temperature was slightly above the Ac_3 temperature for all of the weld frequency cases. No accurate measurement of the weld seam temperature was available for the roll forming apparatus used in this work. After the weld was created, the exterior of the tube is flushed with coolant as a part of the roll forming process.

Table 1. Tubular roll forming weld frequency presented on a relative scale with respect to the LOW sample.

Sample ID	Weld Frequency (Hz)
LOW	1.0
MED	1.17
HIGH	1.26
HIGH_PRF	1.35

2.3. Specimen Preparation

Approximately 300 mm long tubular sections were provided for each of the samples examined in this work. These sections were then cut into ~5 mm thick rings using a wet cut saw in order to prevent heating. The rings were then cut into ~50 mm arc section, with the weld seam centered. These sections were then hot mounted using a conductive phenolic resin. The mounted specimens were first ground using a 220 grit resin bonded disc and then polished using cloth discs and diamond suspensions with the following particle sizes: 9, 3 and 1 µm. Ultrasonic bath cleaning was employed between grinding and polishing stages. In the as-polished state, microhardness measurements were made, which was followed by etching with a 2% Nital solution to reveal the microstructure during scanning electron microscopy (SEM) characterization.

2.4. Microhardness Testing

A Clemex CMT microhardness apparatus was used to conduct all of the hardness testing for this work. For all of the hardness measurements, an indent load of 300 g was selected. Figure 5 shows a schematic of the two different hardness profiles (Centerline and 2D Contour) that were created for this work.

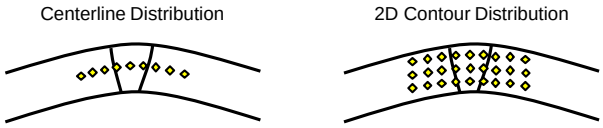

Figure 5. A schematic showing the centerline and 2D contour hardness distributions.

The centerline distribution measurements were made at the mid-plane thickness of the specimens using an indent spacing of 150 µm in order the prevent false measurement due to plastic deformation created by the neighboring indents. After the first centerline distribution measurement was made, the mounted specimens were ground (~1 mm depth), re-polished and the hardness distribution was measured again. This was repeated one more time in order to provide three separate hardness distributions that were then used to create a single average hardness distribution profile.

The automatic x-y stage of the microhardness tester was then used to create a regular grid of hardness indents across the weld seam as shown in the Figure 5 schematic. This grid pattern hardness distribution was then used as input for a MATLAB script that was developed to generate a 2D hardness distribution contour across the weld.

2.5. Scanning Electron Microscopy

A FEI Quanta 250 field emission scanning electron microscope (SEM) was used to generate the micrographs of the various microstructures along the weld seam. These micrographs were created at

known centerline distribution indents for reference. An accelerating voltage of 10 kV was used and the working distance varied from 9.1–9.4 mm for all of the SEM imaging conducted in this work.

2.6. Ring Hoop Tension Test (RHTT)

Dick and Korkolis [34] utilized a Ring Hoop Tensile Test (RHTT) apparatus to measure the hoop flow stress properties of tubular specimens. They implemented 3D digital image correlation (DIC) methods to measure and verify the stress-state within the gauge length of the specimens. They were able to show that because the ring curvature does not change during the test, bending moments and shear forces are zero, allowing for a uniaxial tensile stress-state within the gauge length. This testing approach was adopted to test the weld seam properties for the current work. Figure 6a shows an image of the tubular specimens and the D-block tools that were displaced vertically to deform the ring specimen. A 50 kN electro-mechanical tensile frame was used with a cross-head velocity 0.038 mm/s during the test. The cross-head displacement and axial load were measured for each test up to the point of failure. Petroleum jelly and a thin sheet of Teflon film were used to reduce the friction between the D-blocks and specimen as shown in Figure 6b.

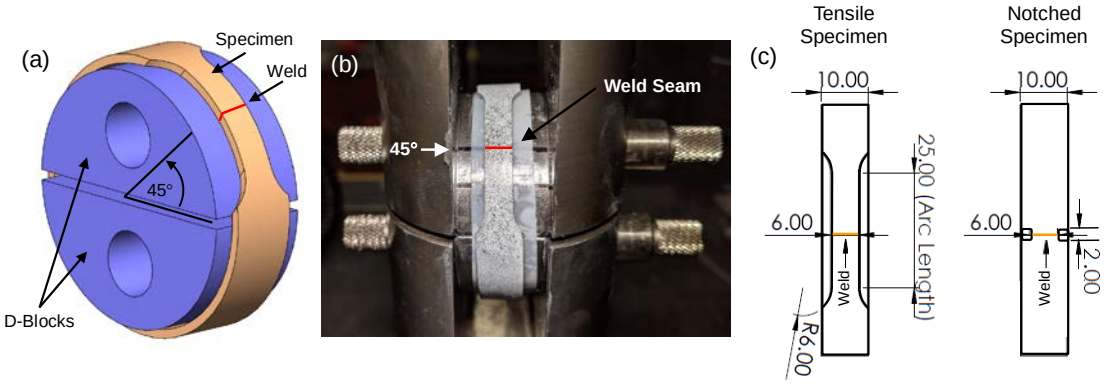

Figure 6. (**a**) A solid model image of the ring hoop tension test (RHTT) tools and specimen used in this work. (**b**) A photograph of a speckled tensile ring specimen with the weld seam shown at the 45° orientation within the RHTT. (**c**) The Tensile and Notched ring specimen geometry used in this work. Dimensions are in mm.

Two different specimens were utilized in the study as shown in Figure 6c. The "Tensile" ring specimen was designed to replicate and ASTM E8 sub-size flat specimen with a gauge length of 25 mm. This specimen was machined with the weld seam located at the middle of the gauge length as indicated in Figure 6c. These specimens were all orientated at 45° to the horizon as shown in Figure 6a,b. In order to force the RHTT deformation within the weld seam region and not the base metal, a "Notched" ring specimen was machined as shown in Figure 6c. The orientation of the weld seam for all of these tests was at 90° to the horizontal. A Correlated Solutions 3D DIC system was used to measure the strain distribution within the Tensile ring specimens only as shown in Figure 6b. It should be noted that all of the welds contained a small weld bead at the inner diameter (ID) of the tubes, after scarfing (roll forming process used to remove majority of ID weld bead). In order to prevent stress concentrations at the weld seam during testing, the weld seam bead was carefully removed using a precision grinder and then polished smooth using 600 grit polishing paper.

3. Results and Discussion

The results of the hardness distribution measurements (centerline and 2D contour), metallographic characterization and the RHTT will be presented and discussed in the following sections.

3.1. Centerline Hardness Distributions

For each of the four induction seam welded specimens presented in Table 1, three repeat centerline hardness measurements were made as shown in Figure 7a–d. By linearly interpolating each of the three repeat distribution measurements at small and equivalent increments, an average hardness distribution curve was generated as shown by the bold and continuous curve in Figure 7a–d. The repeatability of the individual measurements was excellent for the LOW, MED and HIGH_PRF specimens, while the HIGH weld condition had only good repeatability. Figure 7b shows the three distinct zones for these welds, which are the base metal (BM), heat affected zone (HAZ) and the weld zone (WZ). It should be noted that the weld zone terminology used here is synonymous with the fusion zone of a fusion welding process.

3.1.1. Effect of Weld Frequency on Centerline Hardness Distribution

Figure 7e compares the average centerline hardness distributions for the LOW, MED and HIGH weld frequency specimens. Based on this comparison, the LOW and MED weld frequency specimens presented a similar hardness distribution, with some variation at the WZ as will be discussed in a subsequent section. The total weld seam width (HAZ + WZ + HAZ) for the HIGH sample is more narrow than that of the LOW/MED samples for a hardness greater than ~325 HV_{300}. This observation is highlighted in Figure 7f, where the total weld seam width from the average hardness distribution curves in Figure 7e is plotted with respect to hardness (from 300 to 450 HV_{300} only) for the three weld frequency conditions. A simple regression analysis was conducted on the data and a logarithmic fit was applied to the data points in Figure 7f, which confirms the similarity of the LOW/MED weld seam widths and the narrower weld seam width for the HIGH case. The difference in the total weld seam width is due to a narrower WZ for the HIGH sample and a distinct plateau of the hardness distribution at approximately ~325 HV_{300} for the HIGH sample. Qualitatively, Figure 8 shows the narrower HIGH weld seam profile for an etched specimen where the brighter microstructure represents the approximate width of the WZ. It will be shown that the WZ consists of a predominantly martensitic microstructure for all of the welding cases, therefore it is likely that the HIGH weld frequency resulted in a lower welding temperature, which reduced the amount of material at the sheet edge that fully austenitized prior to quenching. Again, it should be repeated that this is a solid-state (or forge) welding process, where the sheet edge does not melt.

3.1.2. Microstructural Analysis of the Weld Seam

The difference in the centerline hardness distribution for the LOW and HIGH case (Figure 7e) is due to the microstructural composition within the HAZ for these two cases. A separate (from Figure 7 data) centerline hardness distribution was measured for these two cases and shown in Figure 9. The mounted samples were then etched and SEM micrographs were created adjacent to the indents which correspond to a common position as denoted as (1) to (4) in Figure 9.

At location (1), a similar mixed ferrite-martensite microstructure exists for both weld cases. Although it must be confirmed using an appropriate quantitative technique (i.e., Electron Backscatter Diffraction), there appears to be some of the original BM retained austenite that is observed as the blocky grains of the featureless constituent.

Location (2) represents the part of the HAZ where the HIGH weld case exhibited a plateau in hardness (Figure 7e), which can also be observed in the Figure 9 centerline hardness distribution. A plateau was not observed in the LOW case, but for this particular location, the hardness was equivalent for both weld cases at 334 HV_{300}. Upon observation of the microstructure at (2), the HIGH weld case microstructure consisted of ferrite-martensite, while the LOW weld case consisted of ferrite, martensite and a third phase which is defined by a ferritic matrix with a fine distribution of carbon rich precipitates that are likely carbides. This phase is labeled (α_C) in Figure 9 and is contained within grains of martensite. Without knowing the temperature-time profile for this complex seam

welding process, it is difficult to hypothesis the precise phases which transform for these solid-state welds. Having said that, similar phases which share the morphologies observed in this work have been reported as coalesced bainite (combined with martensite) in weld microstructures for TRIP [33] and high strength steels [35]. Additionally, researchers have commonly reported this type of phase (combined with martensite) to be auto-tempered martensite within AHSS welds [36,37] and martensitic steels [38,39]. Both coalesced bainite and auto-tempered martensite are formed near the martensite start temperature. It is expected that the strength of the α_C phase is less than martensite, therefore the introduction of α_C and the lower ferrite content in the LOW microstructure allows the hardness of these two microstructures to be equivalent.

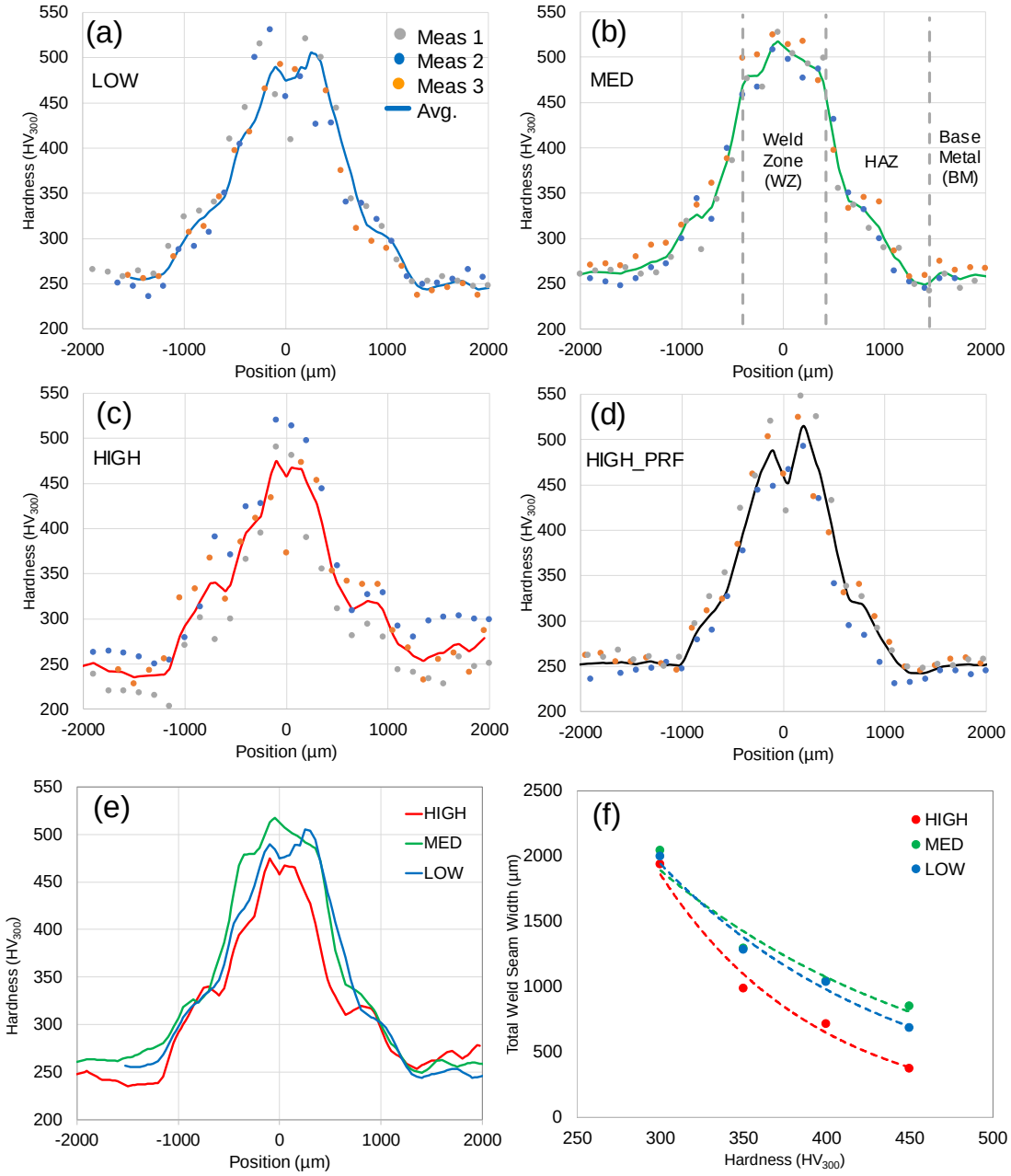

Figure 7. The repeat and average centerline hardness distribution for the (**a**) LOW, (**b**) MED, (**c**) HIGH and (**d**) HIGH_PRF weld specimens. (**e**) A comparison between the average hardness distribution for the different weld frequencies. (**f**) A plot of the average HAZ width versus hardness range for the different weld frequency samples.

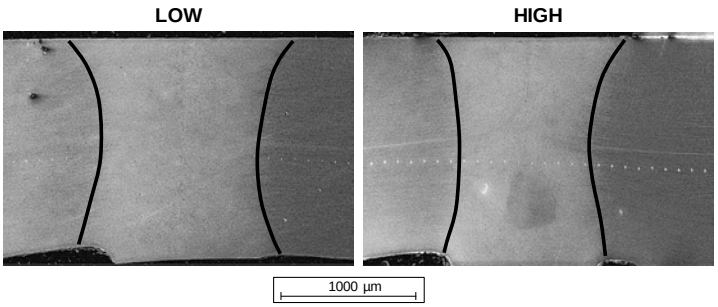

Figure 8. A low magnification SEM micrograph of an etched LOW and HIGH weld frequency case weld.

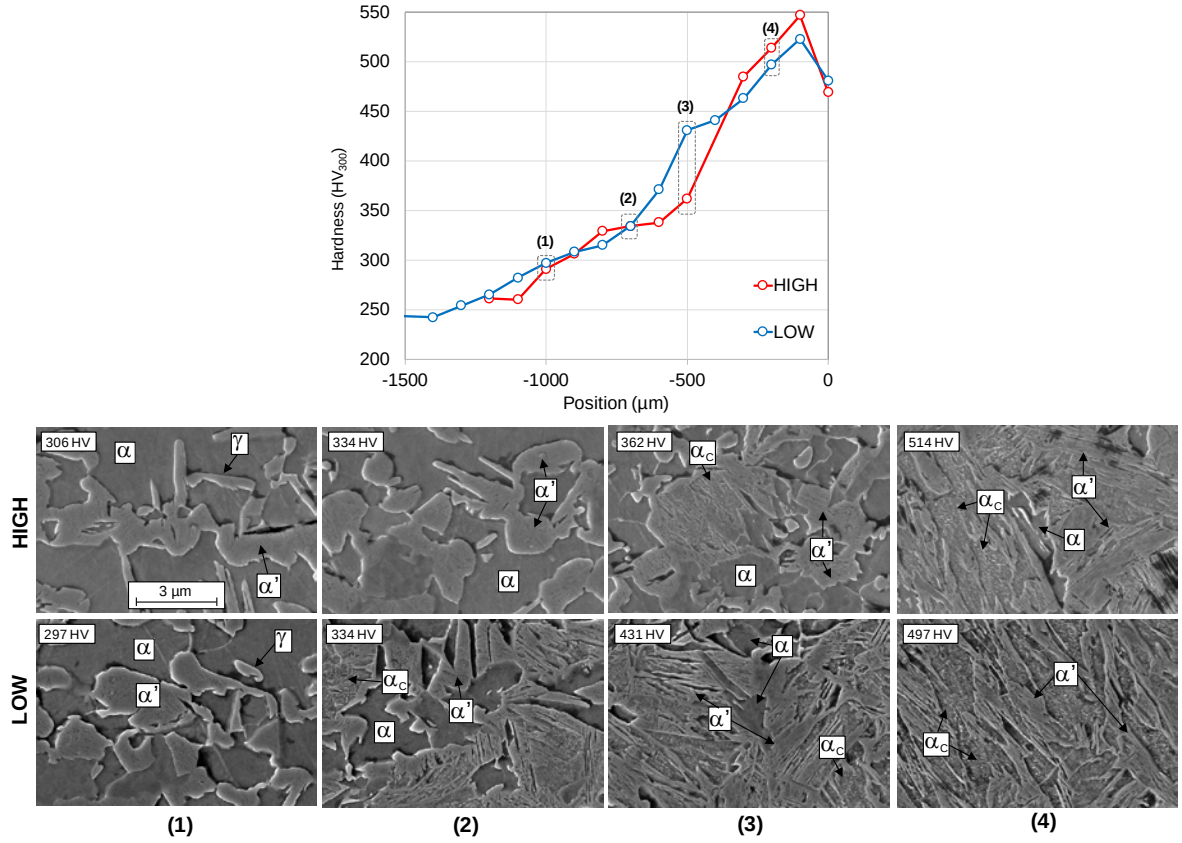

Figure 9. The SEM micrographs at a common position ((1) to (4)) along the centerline hardness distribution for the LOW and HIGH weld frequency cases (α-Ferrite, γ-Retained Austenite, α′-Martensite, α_C-carbide-rich phase). The scale marker is common for all of the micrographs shown.

A large difference in hardness is observed in location (3), where the narrowing of the HIGH weld case was discussed in Section 3.1.1 and shown in Figure 7e–f. The HIGH weld case now has some volume fraction of α_C introduced into the ferrite-martensite microstructure, whereas the LOW weld case is nearly void of ferrite and consists of a predominantly martensitic and α_C microstructure which results in the elevated hardness measurement for this weld frequency case.

Location (4) is at the HAZ-WZ transition for the two cases and consists of a similar martensite and α_C microstructure for both cases as evident by the similar hardness. There is a small volume fraction of ferrite that can be observed (none shown for the LOW case in Figure 9) for both weld cases at this location.

3.1.3. Weld Zone Ferrite-Martensite Band

With the exception of the MED frequency case, the remaining cases all exhibited a local drop in hardness (down to ~400 HV_{300}) within the WZ for some of the repeat measurements as shown in Figure 7a–d. This was unusual because the WZ hardness for all of the cases was ~500 HV_{300} as expected for a predominantly martensitic microstructure. Upon metallographic examination, the local soft region within the WZ was due to the presence of ferrite within the martensitic microstructure as shown in Figure 10. The ferrite-martensite band was ~30 µm in width, therefore it was not detected in some instances due to the spacing of the indents. It is possible that the edge of the tube where the ferrite-martensite band formed (at the weld interface) did not austenitized fully due to either the edge condition of the sheet or the complex magnetic field created through induction for this particular welding setup.

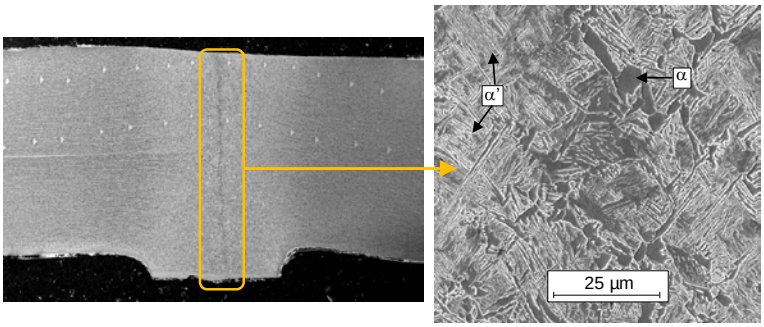

Figure 10. Central ferrite-martensite band within the weld zone (WZ). (α-Ferrite, α'-Martensite).

3.2. 2D Hardness Distribution Contours

For each of the four induction seam welding specimens presented in Table 1, the 2D hardness contour maps of the weld seam region are shown in Figure 11. At first glance, the variation in hardness distribution through the thickness of the sheet is evident among the four different weld conditions examined in this work as discussed in the following.

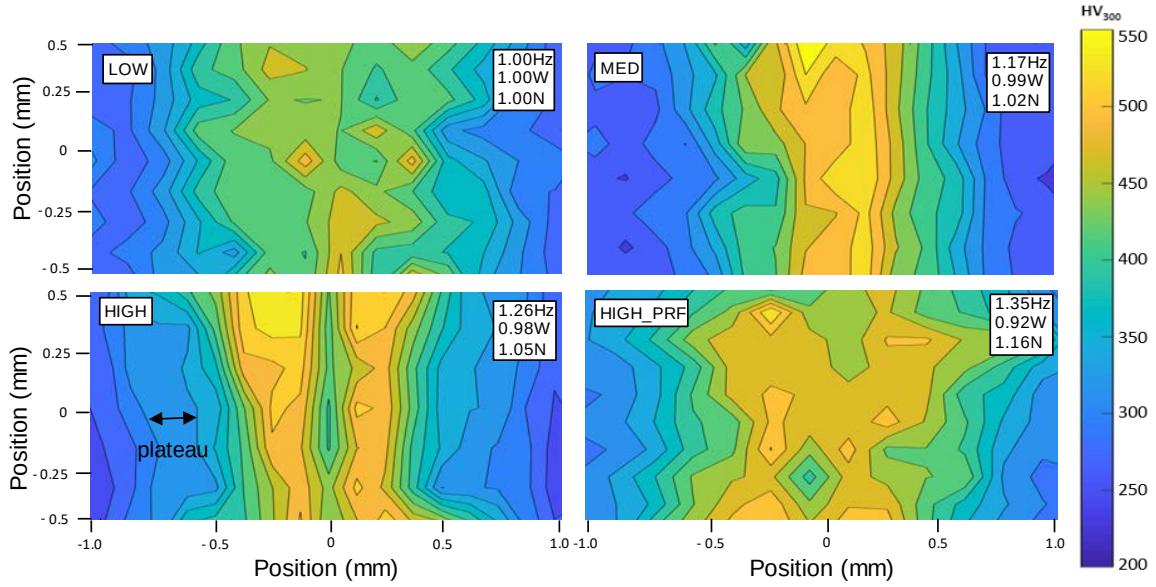

Figure 11. The 2D hardness contour maps for all of the weld conditional examined in this work.

With respect to the center of the weld, only the HIGH frequency case resulted in a relatively symmetric hardness distribution, while the remainder of the weld cases consist of an asymmetric

hardness distribution on either side of the weld. The LOW and HIGH_PRF consisted of local hard regions distributed throughout the WZ and HAZ, which can have an impact on the damage accumulation and fracture performance within these weld seams during deformation. It is also evident that using a single centerline hardness distribution measurement for these types of seam welds does not capture the complex and asymmetric variation in hardness and microstructural distribution for these welds.

The presence of the narrow central martensite-ferrite band was also observed in Figure 11 for the LOW, HIGH and HIGH_PRF weld frequency cases as was shown in centerline hardness distributions (Figure 7) and micrograph (Figure 10). The highest hardness was observed near the top of the weld for the MED, HIGH and HIGH_PRF welds at a value of ~550 HV_{300} which is likely due to an uneven heating of the sheet edge prior to welding, or the higher cooling rate at this surface from the quench media applied during the roll forming process.

The narrower centerline hardness distribution profile of the HIGH frequency (See Figure 7) was also captured by the plateau and steep gradient of hardness contours shown in Figure 11, which is a desirable characteristic of induction seam welds [16]. This narrowing of the WZ and HAZ is consistent through the thickness of the weld. In addition to the asymmetry (with respect to vertical plane) of the LOW and HIGH_PRF, the variation in hardness through the thickness of the welds is high and undesirable from a repeatability perspective as the weld material properties will be inconsistent. Although the total weld seam width (HAZ + WZ + HAZ) of the HIGH_PRF case (Figure 7d) appears to be consistent with the LOW and MED cases, the 2D hardness contour indicates that the high pressure roll force during seam welding resulted in a noticeably wider total weld seam width throughout the thickness of the weld for this particular case. In addition, the average hardness within the wider WZ is relatively high when compared to the other weld seam cases, indicating a wider and higher strength WZ for this case. By comparing the HIGH_PRF and HIGH weld cases, it is evident that an increase in pressure roll force (and frequency in this case) dramatically alters the seam weld characteristics, which is a result of the variation in temperature at the sheet edge (due to frequency) and the effect that the increased force has on the variation in phase transformation kinetics for this particular material.

3.3. Ring Hoop Tension Test (RHTT) Results

The results of the RHTT for the two different specimen geometries (Tensile and Notch) that were considered in this work are presented in the following sections. The LOW, HIGH and HIGH_PRF cases were tested, while the MED welds were not considered due to their similarity to the HIGH case.

3.3.1. Tensile Specimen Results

The force-extension results from the RHTT tests conducted on the Tensile ring specimens are shown in Figure 12a. The LOW and HIGH results are similar with a peak load of ~15.2 kN and an average extension of ~4.8 mm. The HIGH_PRF condition resulted in a lower peak load and extension of 14.3 kN and 3.1 mm, respectively. A second HIGH_PRF repeat test was conducted and showed a similar response. Figure 12b shows the true strain distribution (just prior to fracture) in the y-axis direction (ε_{yy}) as quantified using DIC. For all weld cases, fracture occurred within the base metal (BM), well outside of the seam weld HAZ. Upon further investigation, the lower peak load of the HIGH_PRF weld was due to a reduction in the sheet thickness on the ID of the tube near the weld (due to roll forming setup), which resulted in premature localization of the BM in that region as shown in Figure 12b. The LOW case also exhibited this sheet thinning and localization, but to a lesser degree.

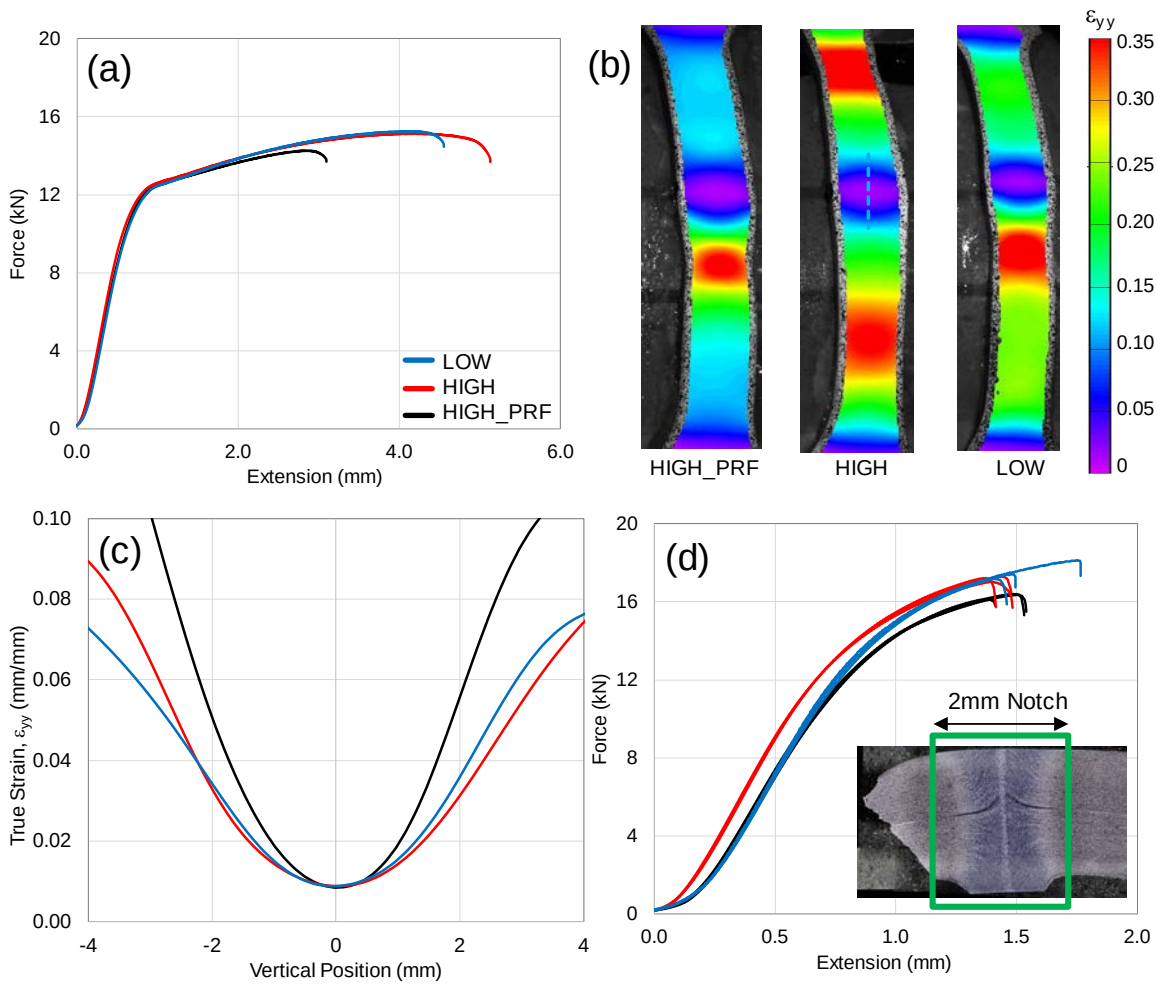

Figure 12. (**a**) The RHTT force-extension curves for the Tensile Specimens. (**b**) The digital image correlation (DIC) contours of true strain in the y-axis (ε_{yy}) just prior to the point of fracture. (**c**) The weld seam strain (ε_{yy}) plotted versus vertical position at a test force of 14 kN. (**d**) The RHTT force-extension curves for the Notch Specimen where three repeat tests are shown for each condition. The 2 mm notch width is indicated in the micrograph.

In order to assess the resistance to deformation of the seam welds, the strain distribution (ε_{yy}) with respect to vertical position (along the vertical dashed line slice shown in Figure 12b, HIGH case) was extracted from the DIC contours for a common test load of 14 kN and is shown in Figure 12c. With the zero vertical position being aligned at the center of the weld seam, the WZ experiences a strain just less than 0.01 for all of the weld cases. Figure 12c also indicates that the microstructural profile of the HIGH_PRF case is less resistant to deformation than the HIGH/LOW cases. This is true for the vertical position range from −1 mm to +1 mm, which represent the total weld seam width (HAZ + WZ + HAZ) and is unaffected by the sheet thinning region discussed above.

3.3.2. Notched Specimen Results

The force-extension results from the RHTT tests conducted on the Notched ring specimens are shown in Figure 12d. The notch width (see Figure 6c) is 2 mm, therefore it encompasses the entire total weld seam width (HAZ + WZ + HAZ) and forces the deformation/fracture to occur within this region, rather than the BM. It should be noted that the distance from the BM-HAZ at one side of the weld to the other is ~2.5 mm, therefore the material condition at the notch is represented by approximately Point 1 in Figure 9. Three repeat test results are plotted with the zero extension point referring to the 0.2 kN load measurement from each test. As a result of the elevated hardness/strength of the seam

welds, all of the peak loads exceeded the peak loads from the Tensile specimens, which failed in the BM. For all three weld conditions, fracture occurred at either end of the notch which is at the interface of the HAZ and BM as indicated by the etched section of a failed HIGH weld case notch in Figure 12d. The HIGH/LOW results were similar at an average peak load of 17.2 kN, while the HIGH_PRF average peak load was slightly lower at 16.3 kN. It is possible that the thinning of the sheet (discussed in Section 3.3.1) for the HIGH_PRF case may have contributed to the lower peak loads. Nonetheless, these three weld cases were sufficient in preventing seam weld fracture and the HIGH/LOW peak forces were 13% greater in these tests when compared to the BM failures from the Tensile specimen tests.

4. Conclusions

As a result of the experimental investigation into the effect of induction seam welding parameters in roll formed TRIP690 tubes, a more thorough understanding has been gained on the impact that induction welding frequency has on the resultant weld seam characteristics, microstructure and fracture performance. The following conclusions can be made:

- Based on the measured centerline hardness distributions, the LOW and MED weld frequency cases resulted in similar hardness distributions, while the HIGH weld frequency resulted in a narrower total weld width within the HAZ due to a plateau in hardness at approximately 325 HV_{300}. The plateau in hardness was due to a delay in the transformation of martensite which indicates that the HIGH weld frequency resulted in a lower weld temperature.
- The HAZ was composed of increasing volume fractions of martensite and coalesced bainite (or auto-tempered martensite) as the hardness increased from the BM towards the WZ. The presence of ferrite was observed within the predominantly martensitic weld interface which may have been due to insufficient austenitization at the complex tube edge condition.
- 2D hardness distributions were shown to be important in identifying highly asymmetric weld microstructure distributions, which are undesirable from a fracture performance perspective.
- An increased weld width was observed for a higher pressure roll force (with changes also to frequency and power) and it is likely that the high weld force resulted in more of the sheet edge being austenitized, but also possibly affected the phase transformation kinetics for this particular grade of TRIP690.
- The Ring Hoop Tension Test (RHTT) was used to evaluate the mechanical weld seam performance of the tubes examined in this work and showed that peak loads were higher for the Notch specimen than the Tensile specimens by ~13% (for HIGH/LOW), indicating good weld fracture performance and the suitability of these tubes for hydroforming applications.
- From an experimental and numerical perspective, future work will focus on quantifying the impact that induction welding parameters have on the complex temperature-time history of the seam welding process. This will allow for the optimization of the weld seam microstructure for this and future novel AHSS.

Author Contributions: Conceptualization, A.B.; methodology, A.B.; formal analysis, A.B.; data curation, B.T.A.; investigation, B.T.A.; writing—original draft, A.B. and B.T.A.; writing—review and editing, A.B.; supervision, A.B.; funding acquisition, A.B. All authors have read and agreed to the published version of the manuscript.

Funding: This research was funded by the Natural Sciences and Engineering Research Council of Canada (NSERC).

Conflicts of Interest: The authors declare no conflict of interest.

References

1. Corporate Average Fuel Economy | NHTSA. (n.d.). Available online: https://www.nhtsa.gov/laws-regulations/corporate-average-fuel-economy#light-duty-stakeholders (accessed on 30 September 2019).
2. Bouaziz, O.; Zurob, H.; Huang, M. Driving force and logic of development of advanced high strength steels for automotive applications. *Steel Res. Int.* **2013**, *84*, 937–947. [CrossRef]

3. Karbasian, H.; Tekkaya, A.E. A review on hot stamping. *J. Process. Technol.* **2010**, *210*, 2103–2118. [CrossRef]
4. Bardelcik, A.; Bouhier, A.; Worswick, M.J. Three Point Bend Performance of Solutionized, Die Quenched and Heat Treated AA7075 Beam Members. *Mater. Sci. Forum* **2014**, *794*, 431–436. [CrossRef]
5. Naka, T.; Yoshida, F. Deep drawability of type 5083 aluminium-magnesium alloy sheet under various conditions of temperature and forming speed. *J. Process. Technol.* **2013**, *89*, 19–23. [CrossRef]
6. Tari, D.G.; Worswick, M.J.; Winkler, S. Experimental studies of deep drawing of AZ31B magnesium alloy sheet under various thermal conditions. *J. Process. Technol.* **2013**, *213*, 1337–1347. [CrossRef]
7. Dohmann, F.; Hartl, C. Tube hydroforming – research and practical application. *J. Process. Technol.* **1997**, *71*, 174–186. [CrossRef]
8. Bardelcik, A. Effect of Pre-Bending and Hydroforming Parameters on the Formability of Advanced High Strength Steel Tube. Master's Thesis, University of Waterloo, Waterloo, ON, Canada, October 2006.
9. Oliveira, D.A. Interaction Between Forming and the Crash Response of Aluminium Alloy S-Rails. Ph.D. Thesis, University of Waterloo, Waterloo, ON, Canada, July 2007.
10. Bardelcik, A.; Worswick, M.J. Evaluation of load control end-feed in hydroforming of pre-bent DP600 steel tube using the extended stress-based forming limit curve failure criterion. *J. Comput. Appl. Mech.* **2006**, *7*, 133–154.
11. Simha, C.H.M.; Gholipour, J.; Bardelcik, A.; Worswick, M.J. Prediction of necking in tubular hydroforming using an extended stress-based forming limit curve. *J. Eng. Mater. Technol.* **2007**, *129*, 36–47. [CrossRef]
12. Groche, P.; Breitenbach, G.V.; Steinheimer, R. Properties of tubular semi-finished products for hydroforming. *Steel Res. Int.* **2005**, *76*, 181–186. [CrossRef]
13. Groche, P.; Breitenbach, G. Roll Forming Strategies for Welded Tubes. *Steel Res. Int.* **2008**, *79*, 40–46. [CrossRef]
14. The Tube and Pipe Journal-Choosing a Welding Process for Tubular Profiles. Available online: https://www.thefabricator.com/tubepipejournal/article/tubepipeproduction/choosing-a-welding-process-for-tubular-profiles (accessed on 15 November 2019).
15. Ghaffarpour, M.; Akbari, D.; Moslemi Naeeni, H.; Ghanbari, S. Improvement of the joint quality in the high-frequency induction welding of pipes by edge modification. *Weld World* **2019**, *63*, 1561–1572. [CrossRef]
16. The Tube and Pipe Journal-Selecting a welding frequency-Research on the optimal frequency for tube production. Available online: https://www.thefabricator.com/tubepipejournal/article/tubepipefabrication/selecting-a-welding-frequency (accessed on 28 January 2020).
17. Weman, K. *Welding processes handbook*, 1st ed.; Woodhead Publishing Ltd.: Cambridge, UK, 2013; p. 89.
18. Nikanorov, A.; Baake, E.; Brauer, H.; Weil, C. Approaches for Numerical Simulation of High Frequency Tube Welding Process. In Proceedings of the International Conference on Heating by Electromagnetic Sources, Pandua, Italy, 22–24 May 2013; pp. 647–654.
19. Kim, C.M.; Kim, J.K. The effect of heat input on the defect phases in high frequency electric resistance welding. *Met. Mater. Int.* **2009**, *15*, 141–148. [CrossRef]
20. Okabe, T.; Yasuda, K.; Nakata, K. Dynamic observations of welding phenomena and finite element analysis in high-frequency electric resistance welding. *Weld. Int.* **2016**, *30*, 835–845. [CrossRef]
21. Li, F.; Ning, J.; Wang, T.; Liang, S.Y. Analytical modeling and sensitivity analysis of the temperature distribution in the planar scanning induction heating based on 2D moving heat source. *J. Mech. Sci. Technol.* **2019**, *33*, 5093–5102. [CrossRef]
22. Li, F.; Ning, J.; Liang, S.Y. Analytical Modeling of the Temperature Using Uniform Moving Heat Source in Planar Induction Heating Process. *Appl. Sci.* **2019**, *9*, 1445. [CrossRef]
23. Zackay, V.F.; Parker, E.R.; Fahr, D.; Busch, R. The enhancement of ductility in high-strength steels. *ASM Trans. Q.* **1967**, *60*, 252–259.
24. Matsumura, O.; Sakuma, Y.; Takechi, H. Enhancement of elongation by retained austenite in intercritical annealed 0.4C-1.5Si-0.8Mn steel. *ISIJ Int.* **1987**, *27*, 570–579. [CrossRef]
25. Ashiri, R.; Mostaan, H.; Park, Y. A Phenomenological Study of Weld Discontinuities and Defects in Resistance Spot Welding of Advanced High Strength TRIP Steel. *Metall. Mater. Trans. A* **2018**, *49*, 6161–6172. [CrossRef]
26. Sajjadi-Nikoo, S.; Pouranvari, M.; Abedi, A.; Ghaderi, A.A. In situ postweld heat treatment of transformation induced plasticity steel resistance spot welds. *Sci. Tchnol. Weld. Joi.* **2018**, *23*, 71–78. [CrossRef]
27. Spena, P.R.; Cortese, L.; De Maddis, M.; Lombardi, F. Effects of Process Parameters on Spot Welding of TRIP and Quenching and Partitioning Steels. *Steel Res. Int.* **2016**, *87*, 1592–1600. [CrossRef]

28. Zhang, M.; Li, L.; Fu, R.; Zhang, J.; Wan, Z. Weldability of Low Carbon Transformation Induced Plasticity Steel. *J. Iron Steel Res. Int.* **2008**, *15*, 61–65. [CrossRef]
29. López Cortéz, V.H.; Pérez Medina, G.Y.; Reyes Valdéz, F.A.; López, H.F. Effects of the heat input in the mechanical integrity of the welding joints welded by GMAW and LBW process in Transformation Induced Plasticity steel (TRIP) used in the automotive industry. *Soldag. insp.* **2010**, *15*, 234–241. [CrossRef]
30. Grajcar, A.; Rózański, M.; Stano, S.; Kowalski, A. Microstructure Characterization of Laser-Welded Mb-Microalloyed Silicon-Aluminum TRIP Steel. *J. Mater. Eng. Perform.* **2014**, *23*, 3400–3406. [CrossRef]
31. Medina, G.P.; Ferreira, H.L.; Robledo, P.Z.; Perez, A.M.; Valdes, F.E.R. Microstructural Development in a TRIP-780 Steel Joined by Friction StirWelding (FSW): Quantitative Evaluations and Comparisons with EBSD. *Soldagem & Inspeção* **2016**, *21*, 146–155. [CrossRef]
32. Mironova, S.; Satoa, Y.S.; Yoneyamab, S.; Kokawaa, H.; Fujiia, H.T.; Hiranoc, S. Microstructure and tensile behavior of friction-stir welded TRIP steel. *Mat. Sci. Eng. A* **2018**, *717*, 26–33. [CrossRef]
33. Mazzaferro, C.C.P.; Ramos, F.D.; Mazzaferro, J.A.E.; de Souza Rosendo, T.; Tier, M.A.D.; da Silva, A.M.; Reguly, A. Microstructure evaluation and mechanical properties of a friction stir spot welded TRIP 800 steel. *Weld. Int.* **2011**, *25*, 683–690. [CrossRef]
34. Dick, C.P.; Korkolis, Y.P. Mechanics and full-field deformation study of the Ring Hoop Tension Test. *Int. J. Solids Struct.* **2014**, *51*, 3042–3057. [CrossRef]
35. Keehan, E.; Karlsson, L.; Bhadeshia, H.K.D.H.; Thuvander, M. Electron backscattering diffraction study of coalesced bainite in high strength steel weld metals. *J. Mater. Sci. Technol.* **2013**, *24*, 1183–1188. [CrossRef]
36. Pouranvari, M.; Sobhani, S.; Goodarzi, F. Resistance spot welding of MS1200 martensitic advanced high strength steel: Microstructure-properties relationship. *J. Manuf. Process.* **2018**, *31*, 867–874. [CrossRef]
37. Saha, D.C.; Biro, E.; Gerlich, A.P.; Zhou, Y. Effects of tempering mode on the structural changes of martensite. *Mat. Sci. Eng. A.* **2016**, *673*, 467–475. [CrossRef]
38. Jarvinen, H.; Honkanen, M.; Jarvenpaa, M.; Peura, P. Effect of paint bake treatment on the properties of press hardened boron steels. *J. Eng. Mater. Technol.* **2018**, *252*, 90–104. [CrossRef]
39. Bourque, C.; Bardelcik, A.; Wells, M.; Chiriac, C. Short cycle tempering of an 1800 MPa grade of press hardening steel. Proceedings of Materials Science and Technology 2019, Portland, OH, USA, 29 September–3 October 2019.